Photocatalytic Performance of Perovskite and Metal–Organic Framework Hybrid Material for the Reduction of N2 to Ammonia

Masoumeh Chamack, Madjid Ifires, Sayed Ali Akbar Razavi, Ali Morsali, Ahmed Addad, Afsanehsadat Larimi, Sabine Szunerits, Rabah Boukherroub

Inorganic Chemistry

pubs.acs.org/IC Article

Photocatalytic Performance of ~~the~~ Perovskite and Metal–Organic Framework Hybrid Material for the Reduction of N_2 to Ammonia

Masoumeh Chamack, Madjid Ifires, Sayed Ali Akbar Razavi, Ali Morsali,* Ahmed Addad, Afsanehsadat Larimi,* Sabine Szunerits, and Rabah Boukherroub*

Cite This: https://doi.org/10.1021/acs.inorgchem.1c03622 Read Online

ACCESS | Metrics & More | Article Recommendations | Supporting Information

ABSTRACT: The orthorhombic phase of $KNbO_3$ perovskite has been applied for nitrogen (N_2) photoreduction to ammonia (NH_3). However, this material suffers from a low surface area and low ammonia production efficiency under UV light irradiation. To eliminate these barriers, we used a metal–organic framework (MOF), named as TMU-5 (~~with formula~~ $[Zn(OBA)(BPDH)_{0.5}]_n$·1.5DMF, where H_2OBA = 4,4′-oxybis(benzoic acid) and BPDH = 2,5-bis(4-pyridyl)-3,4-diaza-2,4-hexadiene), for the synthesis of the $KNbO_3$@TMU-5 hybrid material. $KNbO_3$@TMU-5 achieved a NH_3 production rate of 39.9 $\mu mol \cdot L^{-1} \cdot h^{-1} \cdot g^{-1}$ upon UV light irradiation, as compared to 20.5 $\mu mol \cdot L^{-1} * \cdot h^{-1} \cdot g^{-1}$ recorded for $KNbO_3$ under similar experimental conditions. Using different characterization techniques especially gas adsorption, cyclic voltammetry, X-ray photoelectron spectroscopy, photocurrent measurements, and Fourier transform infrared spectroscopy, it has been found that the higher photoactivity of $KNbO_3$@TMU-5 in ammonia production is due to its higher surface area, higher electron–hole separation efficiency, and higher density of negative charges on Nb sites. This work shows that hybridization of conventional semiconductors (SCs) with photoactive MOFs can improve the photoactivity of the SC@MOF hybrid material in different reactions, especially kinetically complex reactions like photoconversion of nitrogen to ammonia.

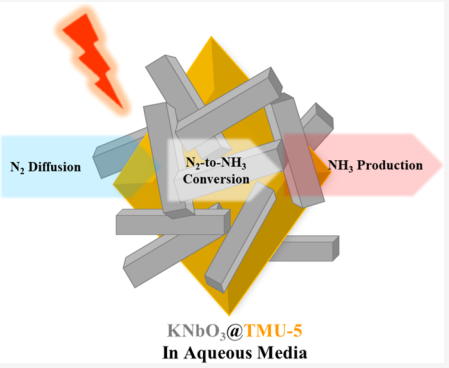

1. INTRODUCTION

Increasing world population and consequent demand for growing agricultural products have led to an increase in demand for ammonia (NH_3), as it represents a basic building block for fertilizer industry. NH_3 is generally produced through the Haber–Bosch process using pure H_2 and N_2 gases under high temperature (>500 °C) and pressure (>200 bar) conditions. Therefore, industrial-scale production of NH_3 requires consumption of large amounts of fossil fuels. In addition to utilizing a large amount of world's energy, industrial production of NH_3 also emits a lot of greenhouse gases every year.[1] In order to address these issues, the last decade has witnessed a huge increase of investigations on the development of low-cost and sustainable photocatalytic processes for NH_3 production.[1−4] In the photocatalytic NH_3 production process, N_2 and H_2O react at room temperature and atmospheric pressure to produce ammonia and O_2 under light irradiation.[1,3] One of the key factors of this process is selecting the appropriate photocatalyst. An ideal photocatalyst for NH_3 production should have some features like facilitated gas diffusion pathway, enhanced adsorption of the reactants, having a band gap energy larger than 1.2 eV with proper band edge position, and activation of molecular nitrogen.[4,5]

Perovskite oxide compounds with the ABO_3 structure play noteworthy roles in various photocatalytic reactions including water splitting into hydrogen, CO_2 photoreduction into fuels, and degradation of organic pollutants and can be regarded as one of the promising candidates for N_2 fixation reaction.[6] However, there are only a few reports on this class of materials for the photocatalytic reduction of N_2. In this regard, the only reported perovskite oxide compounds are $KNbO_3$,[7,8] $LaCoO_3$,[9] $SrTiO_3$,[10] $BiFeO_3$,[11] $LiNbO_3$,[12] and layered Bi_2WO_6.[13,14] Therefore, more investigations are required to understand the aptitude of perovskite oxide materials in the photocatalytic production of NH_3 from N_2.

As a perovskite, $KNbO_3$ can be regarded as a promising photocatalyst for N_2 photoreduction reaction, owing to its proper conduction and valence band positions. The conduction band (CB) and valence band (VB) of $KNbO_3$ are located at around −0.8 and +2.39 eV versus standard hydrogen electrode, respectively (https://doi.org/10.1016/j.apcata.2019.06.001).[7,15] However, the band gap of $KNbO_3$ is in the 3.08–3.24 eV range.[16] Therefore, the best activity for this

Received: November 19, 2021

photocatalyst is achieved under UV irradiation. Furthermore, the specific surface area value, recorded for $KNbO_3$ by means of the N_2 adsorption−desorption technique, is in the range of 0.68 to 3.9 $m^2 g^{-1}$.[16] Such a low surface area might be due to the weak interactions between nitrogen gas molecules and the surface atoms of solid $KNbO_3$, which restricts its photocatalytic applicability in N_2 fixation reaction. To address this hurdle, metal/nonmetal ion doping, noble metal loading, and coupling with SCs have been investigated as approaches for tuning the band gap and surface area of perovskite oxides including $KNbO_3$.[7−14]

To improve the photocatalytic properties of $KNbO_3$, metal−organic frameworks (MOFs) can be appropriate candidates. MOFs, classified as highly porous materials with remarkable potential in adsorption of gas molecules including N_2, can play important roles in enhancing the capability of photocatalysts in N_2 reduction reactions.[17] However, to date, no investigations highlighting the effect of MOF coupling on the photocatalytic properties of $KNbO_3$ have been reported. Furthermore, there are still no ~~study about~~ the effect of coupling of MOFs with perovskite oxides on their photocatalytic operation in N_2 fixation reactions.[6] In spite of increasing gas molecule adsorption, MOFs with the appropriate structure can also improve light absorption, charge separation, and reactant activation, which are expected to lead to superior photocatalytic performance.[18] In this regard, TMU-5 ($[Zn_2(OBA)_2(BPDH)]\cdot(DMF)$) has been described as one of the promising materials with desirable porosity, band gap (2.25 eV) in the visible region, and high specific surface area (591 $m^2 g^{-1}$ based on N_2 adsorption−desorption analysis).[19,20] Additionally, it has been demonstrated that coupling of photoactive TMU-5 to MoO_3 (band gap: 3.2 eV) led to improvement of photodegradation of dibenzothiophene over MoO_3.[20]

In this work, a hybrid material consisting of MOF (TMU-5) and perovskite oxide ($KNbO_3$) is synthesized and applied as a photocatalyst for N_2 fixation reaction, and the effect of coupling of the MOF on the structural properties and photocatalytic performance of the $KNbO_3$ perovskite oxide material has been investigated.

2. EXPERIMENTAL SECTION

2.1. Materials and Instrumentation. *2.1.1. Materials and Methods.* Sodium dodecyl sulfate (SDS, ≥97%), niobium(V) oxide (Nb_2O_5, 99.9%), potassium hydroxide (KOH, 99.99%), 4,4′-oxybisbenzoic acid (oba, 99%), and zinc(II) acetate dihydrate ($Zn(CH_3COO)_2\cdot 2H_2O$, ≥99.0%) were commercially available from Sigma-Aldrich company. Acetonitrile (CH_3CN) and dimethylformamide (DMF, ≥99.9%) were obtained from Merck Company. All materials were used without further purification unless otherwise stated. The ligand 1,4-bis(4-pyridyl)-2,3-diaza-1,3-butadiene (BPDH) was synthesized according to a previously reported method.[21]

The synthesized samples were characterized using various analytical tools. X-ray powder diffraction (XRD) measurements were performed using a Philips X'pert diffractometer with monochromated Cu Kα radiation. N_2 adsorption−desorption isotherms were measured on a Nova Station A instrument at 77 K. The specific surface area was calculated in accordance to the Brunauer−Emmet−Teller (BET) method. The sample for Raman analysis was prepared by dispersing the sample in ethanol by sonication. 50 μL of the solution was drop-cast on a clean silicon wafer and dried. Micro-Raman spectroscopy measurements were recorded on a HORIBA Jobin Yvon LabRam HR micro-Raman system combined with a 473 nm laser diode as the excitation source. Visible light was focused by a 100× objective. The scattered light was collected by the same objective in backscattering configuration, dispersed by an 1800 mm focal length monochromator, and detected by a charge-coupled device (CCD) camera. Scanning electron microscopy (SEM) images were recorded by a Hitachi S-4160 FESEM instrument. Transmission electron microscopy (TEM) images were acquired on a FEI TITAN Themis 300 operating at 300 kV, equipped with a Schottky FEG electron gun and a monochromator. Energy-dispersive X-ray spectroscopy (EDX) analysis was performed with a Philips CM30 microscope operating at 300 kV and equipped with a Brucker EDX detector. X-ray photoelectron spectroscopy (XPS) measurements were recorded with an ESCALAB 220 XL spectrometer from Vacuum Generators, featuring a monochromatic Al Kα X-ray source (1486.6 eV) and a spherical energy analyzer operated in the CAE (constant analyzer energy) mode (CAE = 100 eV for survey spectra and CAE = 40 eV for high-resolution spectra), using the electromagnetic lens mode. No flood gun source was needed due to the conducting character of the substrates. The angle between the incident X-rays and the analyzer was 58°. The detection angle of the photoelectrons was 30°.

2.2. Synthesis Procedures. *2.2.1. Synthesis of $KNbO_3$.* A reported hydrothermal method was used to prepare the $KNbO_3$ material.[22] In short, 36 g of KOH ~~was~~ dissolved in 80 mL of distilled water. 1 g of Nb_2O_5 was added to the alkaline solution and stirred at 50 °C for 30 min. Subsequently, 2.88 g of SDS ~~was~~ added to the mixture and stirred at 50 °C for an additional 30 min. The obtained white color suspension was poured into a 150 mL Teflon-lined stainless-steel autoclave and heated at 180 °C for 48 h. After that, a white solid was formed, separated by centrifugation, and washed with distilled water and ethanol. The obtained $KNbO_3$ powder was dried at 80 °C overnight.

2.2.2. Synthesis of TMU-5. 0.26 g of 4,4′-oxybisbenzoic acid (H_2OBA) was added to 25 mL of DMF and stirred at 80 °C for 30 min. Subsequently, 0.22 g of $Zn(CH_3COO)_2\cdot 2H_2O$ and 0.24 g of BPDH were separately dissolved in 15 mL of DMF. The two solutions were added to the abovementioned mixture and kept under stirring at 80 °C for 72 h. The obtained yellow powder was washed several times with DMF and dried at 80 °C for 24 h. Finally, the prepared MOF was activated by washing it several times with acetonitrile and dried at 120 °C for 72 h. Scheme S1 depicts the structure of TMU-5.

2.2.3. Synthesis of $KNbO_3$@TMU-5. The co-precipitation method was used for the synthesis of the $KNbO_3$@TMU-5 composite. 1 g of $KNbO_3$ powder was added to 50 mL of DMF and sonicated for 5 min. Afterward, 0.5 g of H_2OBA was added to the suspension and the resulting mixture was stirred (500 rpm) at 80 °C for 30 min. Subsequently, 0.44 g of $Zn(CH_3COO)_2\cdot 2H_2O$ and 1 g of BPDH, separately dissolved in 20 mL of DMF, were added to the mixture and the reaction pot was completely sealed. The mixture was stirred at 80 °C for 72 h. The obtained pale yellowish powder was separated by centrifugation, washed several times with DMF, and dried at 80 °C for 24 h. Finally, this sample was activated by the same method as applied for TMU-5. The scheme of the synthesis method is depicted in Scheme S2.

2.3. Preparation of the Modified Electrode. 1 mg of $KNbO_3$@TMU-5 powder was dispersed in 100 μL of ethanol using an ultrasonic bath for 10 min. 3 μl of the dispersed mixture was dripped on ~~the~~ glassy carbon (2 mm diameter) electrode surface and allowed to dry under ~~the~~ IR lamp. Then, 1 μL of nafion solution was added on to the surface and allowed ~~it~~ to dry by the same method. The counter ~~electrode~~ and reference electrode were platinum disk (2 mm diameter) and calomel electrodes, respectively. 10 mL of Na_2SO_4 (0.2 M) was used as the electrolyte solution.

2.4. N_2 Photoreduction Test. *2.4.1. General Photocatalytic Process.* The nitrogen (N_2) photoreduction experiments were performed in a quartz tube. 10 mg of the photocatalyst was added to 10 mL of water and 0.789 mL of ethanol as a hole scavenger. The mixture was dispersed using an ultrasonicator for 10 min, and the resulting suspension was saturated with N_2. During photoreduction under UV irradiation (power of lamp (P) = 0.2 W), N_2 was bubbled into the solution. At certain time intervals, 2 mL of the reaction mixture was collected and immediately centrifuged to separate the liquid sample from the solid catalyst. The concentration of NH_3 was

https://doi.org/10.1021/acs.inorgchem.1c03622
Inorg. Chem. XXXX, XXX, XXX−XXX

measured using the indophenol method via UV−vis absorption spectra recorded using a Safas Bio-UVmc^2 spectrophotometer in quartz cuvettes with an optical path of 10 mm. The wavelength range was 200−800 nm.[23] UV−vis curves of indophenol assays with NH_4^+ ions and the calibration curve used for estimation of NH_3 by NH_4^+ ion concentration are illustrated in Figure S1.

2.4.2. Photocatalytic Stability of $KNbO_3$@TMU-5. The cycling stability of the $KNbO_3$@TMU-5 photocatalyst for N_2 reduction was assessed under UV irradiation. After each cycle, the catalyst was collected by centrifugation, dried in the oven at 60 °C overnight, and reused in the subsequent experiment.

3. RESULTS AND DISCUSSION

3.1. Characterization of Materials. Different instrumental techniques including powder X-ray diffraction (PXRD), nitrogen adsorption at 77 K, XPS, transmission electron spectroscopy (TEM), Fourier transform infrared spectroscopy (FT-IR), Raman spectroscopy, and SEM were applied to characterize the structure of $KNbO_3$@TMU-5.

Combination of PXRD patterns for $KNbO_3$@TMU-5 and its components clearly shows that the structure of both components is identical in their pristine and composite materials (Figure 1). In detail, the PXRD pattern of the

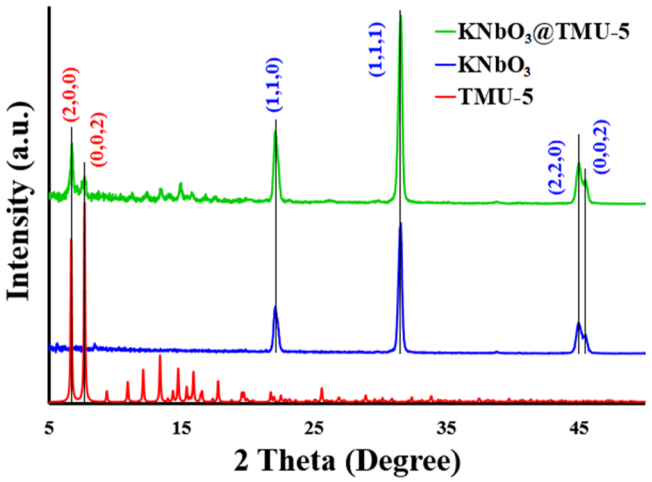

Figure 1. Combination of PXRD patterns of $KNbO_3$@TMU-5 and the components.

TMU-5 MOF comprises two sharp peaks centered at 6.7 and 7.6° indexed respectively to (2,0,0) and (0,0,2) miller indices, which are present in the composite. Also, other relatively weaker bands at 2θ = 12−16° for the TMU-5 sample (12.1, 13.4, 14.7, and 15.9° assigned to (1,1,1), (1,1,−2), (3,1,0), and (3,1,−2), respectively) are observable in the composite. For the $KNbO_3$ sample, XRD peaks observed at 22.1, 31.5, 44.9, and 45.5° are respectively indexed to (1,1,0), (1,1,1), (2,2,0), and (0,0,2) planes of the orthorhombic phase of $KNbO_3$ (space group *Amm*2) (JCPDS card 32-0822),[16] which are observable in the composite, too.

To investigate the role of TMU-5 species in supplying the N_2 reactant for efficient utilization of photoinduced electrons in $KNbO_3$, N_2 adsorption capability of samples was assessed by nitrogen adsorption−desorption measurement at 77 K (Figure 2). For the $KNbO_3$ sample, an isotherm of type III is recorded, which is consistent with nonporous or macroporous solids.[24] For the $KNbO_3$@TMU-5 composite, an isotherm of type I(a) corresponding to microporous materials having mainly narrow micropores (width < ∼1 nm) is observed.[24] The BET surface

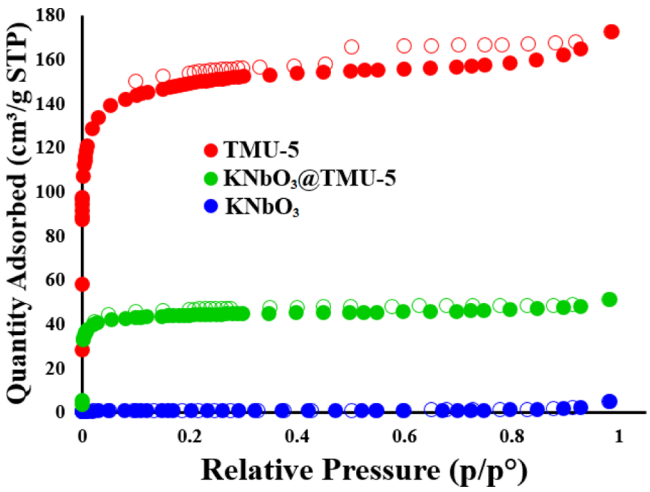

Figure 2. Nitrogen adsorption at 77 K for the $KNbO_3$@TMU-5 composite and its components.

areas, calculated from nitrogen adsorption−desorption isotherms, are about 2 and 172 $m^2 \cdot g^{-1}$ for $KNbO_3$ and $KNbO_3$@TMU-5 samples, respectively. Therefore, compared to pristine $KNbO_3$, the adsorption capacity of the $KNbO_3$@TMU-5 hybrid material for adsorption of N_2 gas molecules was significantly increased. This is a structurally critical improvement for observation enhancement in photocatalytic efficiency of $KNbO_3$@TMU-5 compared to pristine $KNbO_3$, and it can be concluded that TMU-5 can act like a gas cylinder for N_2 storage. TMU-5 can adsorb and store N_2 gas molecules and inject them to the SC surface where the photocatalytic reaction occurs.

XPS was performed to investigate the elemental composition and electronic state of the $KNbO_3$ surface atoms before and after coupling with TMU-5. The full-scan XPS spectra of $KNbO_3$, TMU-5, and $KNbO_3$@TMU-5 are displayed in Figure 3. The XPS spectrum of $KNbO_3$ confirms the presence of

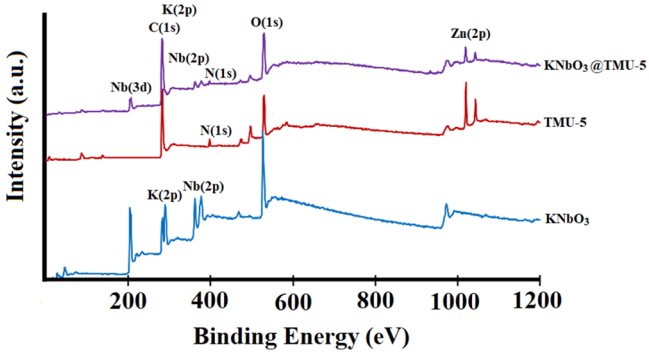

Figure 3. Full-scan XPS spectra of $KNbO_3$, TMU-5, and $KNbO_3$@TMU-5.

potassium, niobium, and oxygen elements. The XPS spectrum of TMU-5 shows the presence of zinc, carbon, oxygen, and nitrogen corresponding to metal ions and linker organic ligands of the MOF. For the $KNbO_3$@TMU-5 spectrum, all peaks related to component elements of both $KNbO_3$ (K, Nb, and O) and TMU-5 (Zn, C, N, and O) are observed.

Besides XPS analysis for $KNbO_3$@TMU-5 and its components, SEM and TEM analyses have been applied to elucidate the morphological structure and structural composi-

https://doi.org/10.1021/acs.inorgchem.1c03622
Inorg. Chem. XXXX, XXX, XXX−XXX

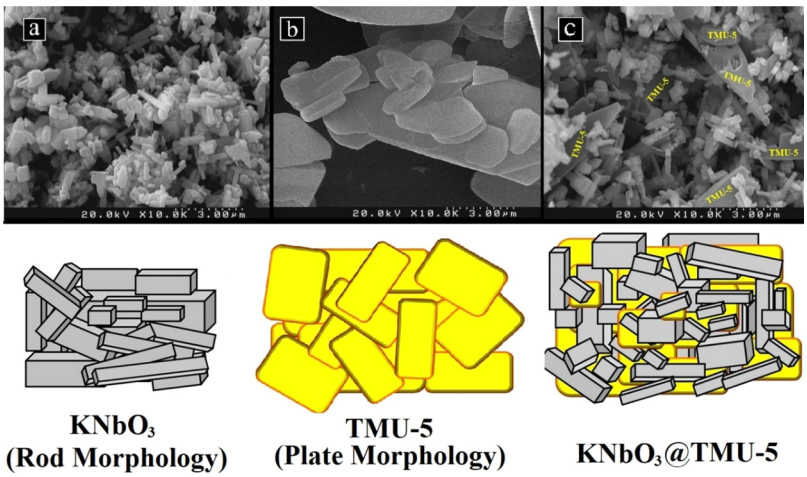

Figure 4. SEM images of $KNbO_3$, TMU-5, and $KNbO_3$@TMU-5. The schemes given below illustrate the morphology of the materials.

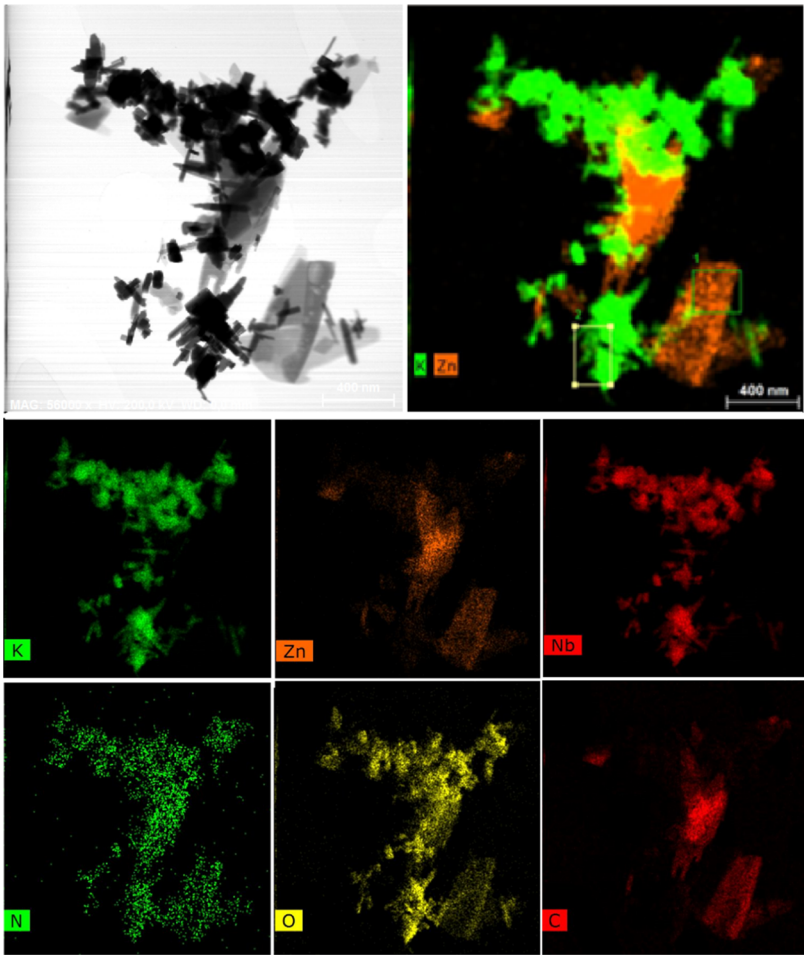

Figure 5. TEM and elemental mapping of $KNbO_3$@TMU-5.

tion of $KNbO_3$@TMU-5 and its components. SEM images clearly show that $KNbO_3$ particles ~~has rod~~ morphology (Figure 4a), while TMU-5 particles are of plate morphology (Figure 4b) in the applied synthesis conditions. These components retain their morphology in the structure of the composite (Figure 4c). TEM elemental mapping images (Figures 5 and S2) ~~display~~ that potassium and niobium elements of $KNbO_3$ are distributed only on the region of tiny rod particles, while the zinc element, originating from TMU-5, is distributed on big blocks' region with plate morphology. The superposition of K and Zn reveals better contrast about the posture of TMU-5 blocks (orange color) and $KNbO_3$ rod particles (green color).

FT-IR spectra of $KNbO_3$, TMU-5, and $KNbO_3$@TMU-5 are depicted in Figure 6. For $KNbO_3$, the sharp broad band below 800 cm^{-1} belongs to Nb−O stretching vibration mode. The FT-IR spectrum of the TMU-5 sample shows vibration modes at 1240 and 1160 cm^{-1} related to C−O−C vibrations.[25] The weak band at 1299 cm^{-1} and the band ranging from 1320 to

https://doi.org/10.1021/acs.inorgchem.1c03622
Inorg. Chem. XXXX, XXX, XXX−XXX

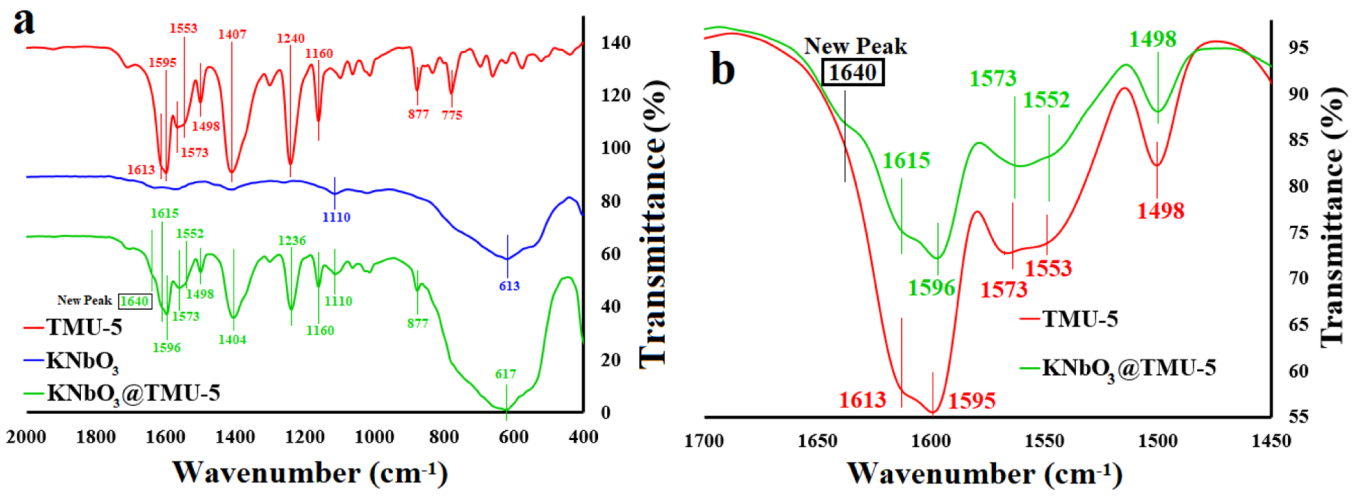

Figure 6. FT-IR ~~spectroscopy for~~ the $KNbO_3$@TMU-5 composite and its components.

1420 cm^{-1} can be attributed to the asymmetric stretching mode of C−O bonds. The peak centered at 1498 cm^{-1} can be assigned to C═N pyridine stretching vibration. The bands centered at 1553 and 1573 cm^{-1} may be due to C═C stretching vibration modes. The bands at 1613 and 1595 cm^{-1} are related to C═N−N═C (azine) and C═N (azomethine) stretching vibration modes, respectively.[25] For $KNbO_3$@TMU-5, all vibration bands of both $KNbO_3$ and TMU-5 are detected with ~~very~~ slight shifts (Figure 6a). Furthermore, a new vibration band appeared at 1640 cm^{-1}, which may be attributed to new C═N vibration mode resulting from interaction between azomethine groups of TMU-5 with the $KNbO_3$ structure (Figure 6b).[26,27] Deconvolution of IR bands ranging from 1450 to 1700 cm^{-1} also displays these details with more clarity (Figure S3).

Compared to the XRD technique, Raman spectroscopy is more sensitive to lattice disorder.[16] Therefore, lattice perturbations in the local structure of NbO_6 octahedra of $KNbO_3$ coupled to TMU-5 were investigated by Raman spectroscopy. Figure 7 depicts the corresponding Raman spectra of $KNbO_3$ and $KNbO_3$@TMU-5 samples. For $KNbO_3$, all the characteristic peaks corresponding to the NbO_6 octahedra appear at the same pattern of the orthorhombic phase reported in literature.[25,27] $B1(TO_2)$, $B1(TO_3)$, $A1(TO_3)$, and $A1(LO_3)$ symmetry modes of NbO_6 are observed at 191.1, 536.9, 594.3, and 834.9 cm^{-1}, respectively. Also, a broad band comprising three vibrating modes of B1(TO1), B1(TO4), and A1(TO1) is detected in the 197−298 cm^{-1} range.[28] The pattern of the orthorhombic phase is also observed for the $KNbO_3$@TMU-5 spectrum, while several new bands are detected above 900 cm^{-1}, which can be related to TMU-5 structure vibration modes. Furthermore, vibration modes of the potassium niobate phase detected in the $KNbO_3$@TMU-5 Raman spectrum revealed slight shifts, as compared to the pristine $KNbO_3$ spectrum. The Raman signal at 191.1 cm^{-1}, attributed to the internal bending vibration mode of the NbO_6 octahedron, experienced a slight shift to 192.7 cm^{-1} for the $KNbO_3$@TMU-5 sample. Also, the shift of O−Nb−O symmetric stretching vibration mode of NbO_6 from 591.5 to 589 cm^{-1} implies its softening due to lowering the bond force constant.[28,29] In contrast, no shift was observed for the band at 536.9 cm^{-1} ascribed to the stretching vibration mode of NbO_6.[16] Moreover, the Raman spectrum of $KNbO_3$@TMU-5 is more broaden than that of $KNbO_3$, suggesting that the lattice disorder of $KNbO_3$ is increased upon coupling with TMU-5. Subsequently, evaluation of Raman spectra suggests the presence of interaction between the TMU-5 and $KNbO_3$ structure in the $KNbO_3$@TMU-5 sample, which affects NbO_6 octahedron vibration modes.[30]

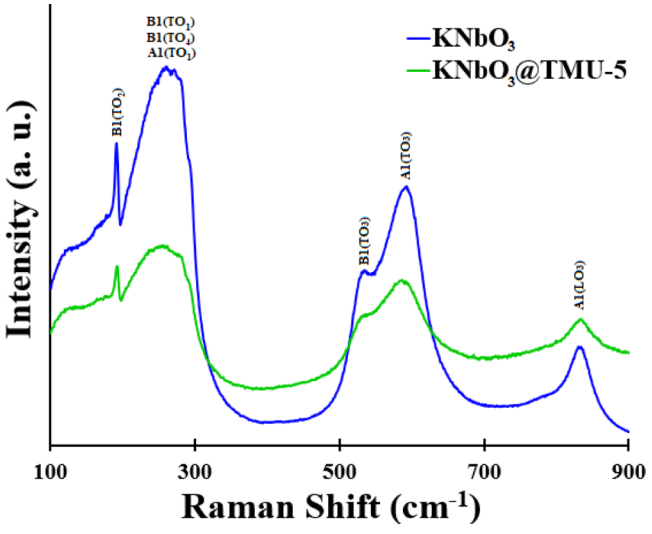

Figure 7. Room-temperature Raman spectra of $KNbO_3$ (blue) and $KNbO_3$@TMU-5 (~~violet~~) samples.

3.2. Photocatalytic Reduction of N_2. The photocatalytic reduction of N_2 to NH_3 comprises several steps. First, like for any other photocatalytic reaction, the photocatalyst absorbs light of appropriate wavelength to generate electron−hole pairs (eq 1). Afterward, a fraction of the photogenerated electrons and holes recombine together, while some holes (h^+) oxidize water into H^+ and O_2 (eq 2) and electrons reduce N_2 to NH_3 (eq 3). Therefore, NH_3 is synthesized from water and N_2 using light as the energy source (eq 4).[2]

$$\text{Photocatalyst} + h\nu \rightarrow h^+ + e^- \quad (1)$$

$$3H_2O + 6h^+ \rightarrow \frac{3}{2}O_2 + 6H^+ \quad (2)$$

$$N_2 + 6H^+ + 6e^- \rightarrow 2NH_3 \quad (3)$$

https://doi.org/10.1021/acs.inorgchem.1c03622
Inorg. Chem. XXXX, XXX, XXX−XXX

$$N_2 + 3H_2O \xrightarrow{h\nu} 2NH_3 + \frac{3}{2}O_2 \quad (4)$$

Even though any photocatalyst having a band gap energy larger than 1.2 eV with proper CB and VB positions can thermodynamically promote the reaction of eq 3, this half-reaction is kinetically more challenging because of the required six electrons. Furthermore, the adsorption of N_2 gas molecules over the photocatalyst surface and cleavage of the highly stable N≡N bond are also regarded as remarkable challenges.[2] To address these issues, coupling of the photocatalyst with MOFs having high capacity for N_2 gas molecule adsorption, which can modify the electron transfer mechanism in the photocatalyst, could represent a promising strategy.[18,31] Apart from enhancement in adsorption capacity, many investigations demonstrated that coupling of a SC with MOFs can modify the electronic structure of the SC, leading to enhanced performance for various photocatalytic reactions including water splitting, CO_2 reduction, and organic pollutant degradation.[18] Nevertheless, for N_2 photo−reduction reaction, there are still a few reports about the role of MOFs in improving the SCs' photocatalytic activity. Hence, for improvement of the operation of $KNbO_3$ through enhancement in adoption capacity and photocatalytic activity, it has been coupled to TMU-5 to synthesize the $KNbO_3$@TMU-5 hybrid material.

The photocatalytic activity of the as-synthesized $KNbO_3$ and $KNbO_3$@TMU-5 samples for the reduction of N_2 to NH_3 in the presence of water is illustrated in Figure 8. Without light

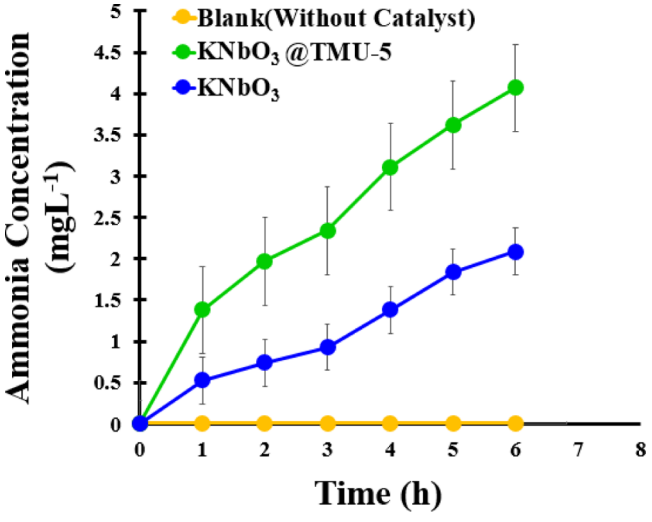

Figure 8. N_2 reduction to ammonia efficiency as a function of irradiation time under UV illumination.

irradiation (blank test), no NH_3 was formed by adding $KNbO_3$ or $KNbO_3$@TMU-5 catalysts to N_2-saturated aqueous solution (Figure S4). Under UV light irradiation, the NH_3 generation rate reaches 20.5 $\mu mol \cdot L^{-1} \cdot h^{-1} \cdot g^{-1}$ in the presence of the $KNbO_3$ photocatalyst, while by applying $KNbO_3$@TMU-5, the NH_3 generation rate increased to 39.9 $\mu mol \cdot L^{-1} \cdot h^{-1} \cdot g^{-1}$. To examine the reusability of the $KNbO_3$@TMU-5 photocatalyst, the N_2 reduction system was recycled five times (Figure 9). During the first three cycles of the reaction, NH_3 production efficiency was not changed. However, after the fifth run, the NH_3 production rate is 37.9 $\mu mol \cdot L^{-1} \cdot h^{-1} \cdot g^{-1}$, confirming the high stability of the developed photocatalyst. Table S1 compares the rate of nitrogen reduction for $KNbO_3$@TMU-5 with some of other MOF-based photocatalysts applied in this area.

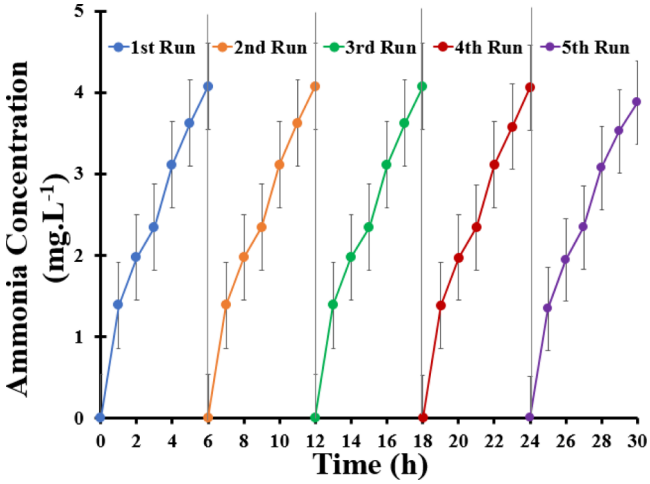

Figure 9. Photocatalytic stability of $KNbO_3$@TMU-5 during five cycling tests.

To investigate the effect of coupling of TMU-5 on the charge transfer and recombination behavior of $KNbO_3$, photoluminescence measurements were employed at an excitation wavelength of 325 nm. As shown in Figure S5, the $KNbO_3$ sample exhibited a strong blue luminescence emission in the 350−455 nm range, which may be attributed to the emission connected with charge transfer from oxygen atoms to the central niobium atom in the NbO_6 octahedra. The luminescence emission was observed for the $KNbO_3$@TMU-5 sample with relatively lower intensity compared to pristine $KNbO_3$, suggesting that TMU-5 hybridization with $KNbO_3$ reduces the recombination rate of photogenerated electron−hole pairs, which may be due to the internal charge transfer between the $KNbO_3$ and TMU-5 component.[32] A complementary study on electron−hole separation by photocurrent measurement demonstrates that the rate of charge recombination is significantly diminished upon hybridization of $KNbO_3$ with TMU-5 (Figure S6). These results clearly show that the photoactivity of the $KNbO_3$@TMU-5 composite is highly improved compared to pristine $KNbO_3$.

To investigate the effect of TMU-5 on the optical properties of $KNbO_3$, UV−vis analysis was performed (Figure S7). The optical band gap (E(bg)) of $KNbO_3$ and $KNbO_3$@TMU-5 samples was determined using the following equation (eq 5):

$$(\alpha h\nu)^n = A(h\nu - E(bg)) \quad (5)$$

where α, h, ν, A, and E(bg) represent the absorption coefficient, Planck constant, light frequency, proportionality constant, and band gap, respectively. The value of n depends on the nature of the electronic transition and assumed to be 1/2 for $KNbO_3$, which has an indirect band gap. By plotting $(\alpha h\nu)^{1/2}$ versus $(h\nu)$, E(bg) can be estimated from the intercept of the tangent to the x-axis.[28] Accordingly, an E(bg) value of 3.2 eV (387.45 nm) was calculated for $KNbO_3$, which is in good agreement with previous reports.[28,33] After hybridization of $KNbO_3$ with TMU-5, the E(bg) value decreased slightly to 3.1 eV (399.95 nm).

In the next step, the Mott−Schottky diagram has been drawn to calculate the flat band potentials (E(fb)) of TMU-5 and $KNbO_3$ components to calculate their CB and VB energy levels (Figure S8). The calculated E(fb) values for TMU-5 and

https://doi.org/10.1021/acs.inorgchem.1c03622
Inorg. Chem. XXXX, XXX, XXX−XXX

$KNbO_3$ are −1.4 V and −0.7 V, respectively. In a general verified approximation for n-type photocatalysts, energy levels of CB and VB can be calculated based on following equations (eqs 6 and 7).

$$E_{CB} = E(\text{fb}) - 0.2 \quad (6)$$

$$E_{VC} = E_{CB} + E(\text{bg}) \quad (7)$$

According to the values of E(fb) and E(bg) for TMU-5 and $KNbO_3$ (Table S2), the mechanistic diagram of photoreduction of nitrogen by $KNbO_3$@TMU-5 is depicted in Figure 10.

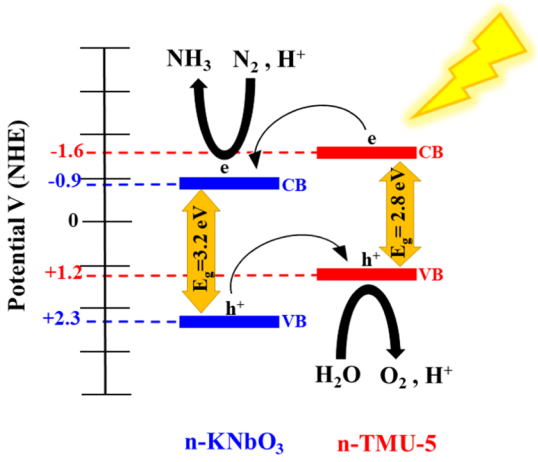

Figure 10. Energy levels of TMU-5 and $KNbO_3$ and mechanism of nitrogen reduction by $KNbO_3$@TMU-5.

3.3. Mechanism of Nitrogen Reduction. XPS analysis is an ideal technique for characterization of a material before and after coupling with another component in a composite. In this regard, XPS analysis applied to understand the electronic state of the $KNbO_3$' atoms before and after coupling with TMU-5. The core-level XPS spectra for Zn, C, K, and O and especially Nb and N atoms were collected.

The core-level spectra of Zn 2p of TMU-5 and $KNbO_3$@TMU-5 are displayed in Figure S9. The Zn 2p spectrum of TMU-5 contains a doublet at binding energies (BEs) of 1019.3 and 1042.4 eV assigned to $Zn2p_{3/2}$ and $Zn2p_{1/2}$ lines, respectively.[19] These values observed in case of $KNbO_3$@TMU-5, too.

The core-level scans of the C 1s of $KNbO_3$, TMU-5, and $KNbO_3$@TMU-5 samples are illustrated in Figure S10. A sharp peak for the $KNbO_3$ sample situated at 284.9 eV is observed and can be assigned to the adventitious carbon. For TMU-5, the spectrum can be curve-fitted by three components at 284.9, 286.2, and 288.6 eV ascribed respectively to the sp^2-hybridized carbon including aromatic carbon (−C═C), carbon-nitrogen or carbon-oxygen bonds, and (O−C═O) bonds.[34] The C 1s spectrum of the $KNbO_3$@TMU-5 sample is also deconvoluted into three peaks at 284.9 eV (C═C), 285.8 eV (C−N/C−O), and 288.6 (O−C═O) eV.

For the $KNbO_3$ sample, the BEs of K $2p_{3/2}$ and $K2p_{1/2}$, illustrated in Figure S11, are close to 291.0 and 293.7 eV, respectively. A positive shift (0.7 eV) is observed for the $KNbO_3$@TMU-5 sample that can be due to the decrease of potassium electron density after coupling of $KNbO_3$ to TMU-5.[35]

Based on XPS measurements (Figure 11), Nb $3d_{5/2}$ and Nb $3d_{3/2}$ of $KNbO_3$ are located at 206.5 and 209.3 eV,

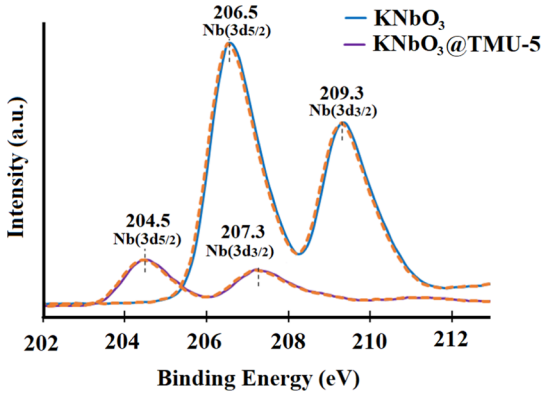

Figure 11. Core-level XPS scan of Nb atoms for $KNbO_3$ and $KNbO_3$@TMU-5.

respectively, with a spin−orbit splitting of 2.8 eV. After hybridization of TMU-5 with $KNbO_3$, the Nb $3d_{5/2}$ and Nb $3d_{3/2}$ core-level binding energies (BEs) shifted to 204.5 and 207.3, respectively. According to the literature, this negative shift can be ascribed to electron transfer to Nb atoms.[36]

As shown in Figure 12, for the TMU-5 sample, the N 1s XPS sharp peak can be fitted to the C═N group (397.9 eV). The C═N peak is shifted to 397.1 eV in the $KNbO_3$@TMU-5 hybrid material.[34] The weak peaks centered at 399.2 eV for both TMU-5 and $KNbO_3$@TMU-5 samples can be ascribed to pyridine nitrogen of the BPDH ligand of TMU-5. These results show that upon formation of the $KNbO_3$@MU-5 composite, the electronic properties of N atoms of coordinating pyridine groups did not change, while an alteration in electronic properties of N atoms of azine function (−C═N−N═C−) is observed.

The O 1s XPS spectra of $KNbO_3$ and $KNbO_3$@TMU-5 are displayed in Figure S12. For $KNbO_3$, the spectrum can be deconvoluted into three components at 529.4, 530.2, and 531.7 eV due to oxygen of perovskite lattice, oxygen deficient bonding, and weakly bound O^- and OH^- surface species, respectively (Figure S12a). The O 1s XPS spectrum of TMU-5 is fitted with two components at 529.8 and 531.4 eV, which can be assigned to carboxylate and ether groups of the OBA^{2-} ligand of TMU-5, respectively (Figure S12b). The spectrum of the $KNbO_3$@TMU-5 sample can be curve-fitted with four components at 527.2, 529.2, 531.1, and 531.9 eV (Figure S12c).[37] Compared to O 1s XPS spectra of $KNbO_3$ and TMU-5 samples, a new peak centered at 527.2 eV (O* atom in Figure S12c) is observed for $KNbO_3$@TMU-5.

Overall, based on the observed shifts in XPS analysis of TMU-5 and $KNbO_3$ samples before and after hybridization in the $KNbO_3$@TMU-5 composite, it is possible to say that the significant changes in oxidation numbers are observed in the case of Nb and N atoms. These changes are discussed in detail as follows. For this purpose, the required information from FT-IR and XPS analyses is gathered here and discussed together.

As is mentioned, Nb(3d) core-level XPS analysis shows that the BE for Nb atoms shifts is equal to 2 eV after synthesis of $KNbO_3$@TMU-5, while the value of spin−orbit coupling (2.8 eV) does not alter. Because such a shift in the BE of Nb atoms occurs after hybridization of $KNbO_3$ with TMU-5, it is rational to hypothesize that there is some kind of interactions between

https://doi.org/10.1021/acs.inorgchem.1c03622
Inorg. Chem. XXXX, XXX, XXX−XXX

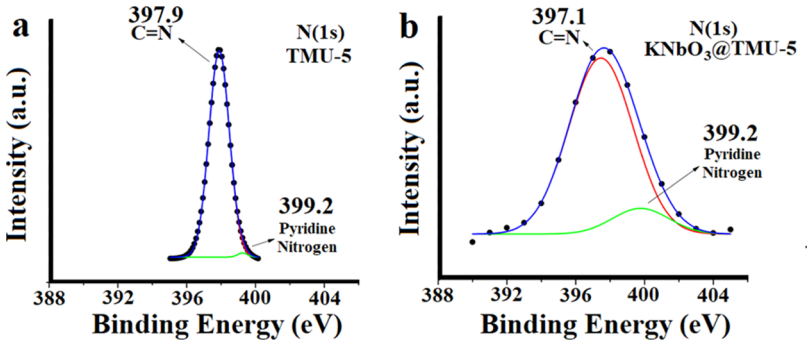

Figure 12. Core-level XPS scan of N atoms for TMU-5 (a) and $KNbO_3$@TMU-5 (b).

these two materials in the final composite. Based on N(1s) core-level XPS, it has been observed that there is a positive shift equal to 0.8 eV in the BE of the azine −C═N− site, while the binding energy of pyridine −C═N− is completely unchanged. Based on core-level XPS analysis of N and Nb atoms, it is possible to state that Nb sites of $KNbO_3$ and azine functions (−C═N−N═C−) of TMU-5 are potential interactive sites after the formation of the $KNbO_3$@TMU-5 photocatalyst.

The mentioned assumption, possible interaction between Nb^{+5} centers and azine sites in the composite, can be witnessed using FT-IR spectroscopy specifically in the 1450−1700 cm^{-1} region. Based on the literature, this region belongs to ~~observation~~ of −C═N− bonds. As can be seen in Figure 6b, there is a new peak centered at 1640 cm^{-1} after the formation of the $KNbO_3$@TMU-5 composite, while other peaks (related to pyridine C═N, aromatic C═C, azomethine −C═N− and azine −C═N−N═C− bonds) are almost identical. According to the literature, FT-IR analysis of aromatic azine function shows a singlet peak ~~at~~ the 1600−1635 cm^{-1} region,[38] similar to what we observed here, 1613 cm^{-1} for TMU-5 and 1615 cm^{-1} for the composite. In the cases that there is a specific interaction between azine −C═N−N═C− bonds and metal, a new peak can be observed in the 1630−1652 cm^{-1} region.[39] Therefore, according to shifts in XPS peaks of Nb atoms along with the formation of a new band at 1640 cm^{-1} in FT-IR, we reason that there is specific kind of interaction between azine functions of TMU-5 and Nb^{+5} sites of KNbO3 in the composite. Based on principles of XPS measurement, the BE of a specific atom will decrease if the density of negative charges is increased on that specific atom. Therefore, due to the shift in the BE of Nb^{+5} sites to the lower values, it can be speculated that the density of negative charges is increased on Nb^{+5} sites. The final values of BE of Nb sites in the composite is relatively similar to Nb^{+4} species published in the literature.[40−42] This higher negative charge density on Nb sites is another reason for improvement of N_2 reduction efficiency in case of $KNbO_3$@TMU-5 compared to pristine $KNbO_3$. Cyclic voltammetry ~~has been~~ conducted to compare the reducing strength of $KNbO_3$ before and after hybridization (Figure S13). The results show that the reduction reaction on $KNbO_3$@TMU-5 shifts to more positive reduction potentials as equal as 60 mV (from −770 to −710 mV), which indicates that the $KNbO_3$@TMU-5 composite has higher affinity to reduction reactions compared to $KNbO_3$.

Therefore, $KNbO_3$@TMU-5 is a more efficient photocatalyst for reductive photoconversion of nitrogen molecules to ammonia. Overall, there are three major reasons that assist $KNbO_3$@TMU-5 to show higher efficiency compared to pristine $KNbO_3$, which are (I) increased porosity and surface area, (II) higher efficiency in photoinduced electron−hole separation, and (III) higher density of negative charges on Nb sites in the composite. Based on these reasons, the mechanism of nitrogen photoreduction by $KNbO_3$@TMU-5 can be described in detail as follows. In the first step, N_2 molecules access the surface of $KNbO_3$ through diffusion in the three-dimensional interconnected pores of TMU-5. In this condition, it can be stated that the pores of TMU-5 act as nanocylinders to accumulate the surface of $KNbO_3$ ~~with nitrogen molecules~~. Due to the higher surface area of $KNbO_3$@TMU-5 than pristine $KNbO_3$, it is anticipated that the concentration of N_2 molecules on the surface of $KNbO_3$ is more than that on pristine $KNbO_3$. In the next step, upon light irradiation, the organic framework of TMU-5 is used as antenna and absorbs light photons, which improves the electron−hole separation efficiency of $KNbO_3$@TMU-5, becoming higher than that of pristine $KNbO_3$. The higher the charge carrier separation, the higher will be the photocatalytic efficiency. In the final step, it is anticipated that the rate of N_2 reduction will increase due to the changes in BEs and higher affinity of Nb sites to the reduction reaction in the composite after hybridization of $KNbO_3$ with TMU-5 in the composite. Therefore, the rate of ammonia production will increase for $KNbO_3$ in the composite form when compared to the pristine form.

CONCLUSIONS

$KNbO_3$ is one of the perovskite-based SCs that was used for photocatalytic nitrogen reduction. However, it has some disadvantages like no porosity and band gap in the UV reg on. To overcome these challenges, we have synthesized a hybrid material based on $KNbO_3$ and one of our TMU MOFs named as TMU-5 because it is porous to nitrogen molecules and its optical band gap lies in the visible region. Experimental analyses suggest that there are three reasons for improved photocatalytic activity of $KNbO_3$ in the $KNbO_3$@TMU-5 composite when compared to the pristine material. The higher surface area and porosity of the composite compared to pristine $KNbO_3$, higher affinity of Nb sites to reduction reaction in the composite due to the changes in BEs after hybridization, and higher efficiency in electron−hole separation in the composite ~~are the major reasons for improved photocatalytic activity of the KNbO3@TMU-5 composite when compared to pristine KNbO3~~.

https://doi.org/10.1021/acs.inorgchem.1c03622
Inorg. Chem. XXXX, XXX, XXX−XXX

■ ASSOCIATED CONTENT

Supporting Information

The Supporting Information is available free of charge at https://pubs.acs.org/doi/10.1021/acs.inorgchem.1c03622.

TMU-5 framework scheme, TEM images, deconvoluted FT-IR spectrum, blank photocatalytic tests, photoluminescence and photocurrent measurements, Tauc plots, Mott−Schottky diagrams, and XPS measurements (PDF)

■ AUTHOR INFORMATION

Corresponding Authors

Ali Morsali − *Department of Chemistry, Faculty of Sciences, Tarbiat Modares University, Tehran 14117-13116, Islamic Republic of Iran*; orcid.org/0000-0002-1828-7287; Phone: (+98) 21-82884416; Email: morsali_a@modares.ac.ir

Afsanehsadat Larimi − *Department of Chemical and Process Engineering, Niroo Research Institute, Tehran 14686-13113, Iran*; orcid.org/0000-0001-5566-171X; Email: Alarimi@nri.ac.ir

Rabah Boukherroub − *Universityof Lille, CNRS, Centrale Lille, Université Polytechnique Hauts-de-France, UMR 8520, IEMN, Lille F-59000, France*; Email: rabah.boukherroub@univ-lille.fr

Authors

Masoumeh Chamack − *Department of Chemistry, Faculty of Sciences, Tarbiat Modares University, Tehran 14117-13116, Islamic Republic of Iran*

Madjid Ifires − *Universityof Lille, CNRS, Centrale Lille, Université Polytechnique Hauts-de-France, UMR 8520, IEMN, Lille F-59000, France; Research Center of Semiconductor Technology for Energy, Merveilles 16038, Algeria*

Sayed Ali Akbar Razavi − *Department of Chemistry, Faculty of Sciences, Tarbiat Modares University, Tehran 14117-13116, Islamic Republic of Iran*

Ahmed Addad − *University of Lille, CNRS, UMR 8207—UMET, Lille F-59000, France*

Sabine Szunerits − *Universityof Lille, CNRS, Centrale Lille, Université Polytechnique Hauts-de-France, UMR 8520, IEMN, Lille F-59000, France*; orcid.org/0000-0002-1567-4943

Complete contact information is available at: https://pubs.acs.org/10.1021/acs.inorgchem.1c03622

Notes

The authors declare no competing financial interest.

■ ACKNOWLEDGMENTS

National Centre for Scientific Research (CNRS), Center for International Scientific Studies and Collaboration (CISS), The University of Lille, the Hauts-de-France region, Tarbiat Modares University (TMU), and Niroo Research Institute (NRI) are gratefully acknowledged for financial support.

■ REFERENCES

(1) Chen, X.; Li, N.; Kong, Z.; Ong, W.-J.; Zhao, X. Photocatalytic fixation of nitrogen to ammonia: state-of-the-art advancements and future prospects. *Mater. Horiz.* **2018**, *5*, 9−27.

(2) Vu, M.-H.; Sakar, M.; Do, T.-O. Insights into the recent progress and advanced materials for photocatalytic nitrogen fixation for ammonia (NH3) production. *Catalysts* **2018**, *8*, 621.

(3) Shi, R.; Zhao, Y.; Waterhouse, G. I. N.; Zhang, S.; Zhang, T. Defect engineering in photocatalytic nitrogen fixation. *ACS Catal.* **2019**, *9*, 9739−9750.

(4) Chen, S.; Liu, D.; Peng, T. Fundamentals and Recent Progress of Photocatalytic Nitrogen-Fixation Reaction over Semiconductors. *Sol. RRL* **2021**, *5*, 2000487.

(5) Comer, B. M.; Medford, A. J. Analysis of photocatalytic nitrogen fixation on rutile TiO2 (110). *ACS Sustainable Chem. Eng.* **2018**, *6*, 4648−4660.

(6) Kumar, A.; Kumar, A.; Krishnan, V. Perovskite oxide based materials for energy and environment-oriented photocatalysis. *ACS Catal.* **2020**, *10*, 10253−10315.

(7) Xing, P.; Wu, S.; Chen, Y.; Chen, P.; Hu, X.; Lin, H.; Zhao, L.; He, Y. New application and excellent performance of Ag/KNbO3 nanocomposite in photocatalytic NH3 synthesis. *ACS Sustainable Chem. Eng.* **2019**, *7*, 12408−12418.

(8) Xing, P.; Zhang, W.; Chen, L.; Dai, X.; Zhang, J.; Zhao, L.; He, Y. Preparation of a NiO/KNbO 3 nanocomposite via a photodeposition method and its superior performance in photocatalytic N 2 fixation. *Sustain. Energy Fuels* **2020**, *4*, 1112−1117.

(9) Zhang, H.; Li, X.; Su, H.; Chen, X.; Zuo, S.; Yan, X.; Liu, W.; Yao, C. Sol−gel synthesis of upconversion perovskite/attapulgite heterostructures for photocatalytic fixation of nitrogen. *J. Sol-Gel Sci. Technol.* **2019**, *92*, 154−162.

(10) Tao, R.; Li, X.; Li, X.; Shao, C.; Liu, Y. TiO 2/SrTiO 3/gC 3 N 4 ternary heterojunction nanofibers: gradient energy band, cascade charge transfer, enhanced photocatalytic hydrogen evolution, and nitrogen fixation. *Nanoscale* **2020**, *12*, 8320−8329.

(11) Mansingh, S.; Sultana, S.; Acharya, R.; Ghosh, M. K.; Parida, K. M. Efficient photon conversion via double charge dynamics CeO2−BiFeO3 p−n heterojunction photocatalyst promising toward N2 fixation and phenol−Cr (VI) detoxification. *Inorg. Chem.* **2020**, *59*, 3856−3873.

(12) Li, X.; He, C.; Dai, D.; Zuo, S.; Yan, X.; Yao, C.; Ni, C. Nanomineral induced nonlinear optical LiNbO 3 with abundant oxygen vacancies for photocatalytic nitrogen fixation: boosting effect of polarization. *Appl. Nanosci.* **2020**, *10*, 3477−3490.

(13) Zhang, C.; Chen, G.; Lv, C.; Yao, Y.; Xu, Y.; Jin, X.; Meng, Q. Enabling nitrogen fixation on Bi2WO6 photocatalyst by c-PAN surface decoration. *ACS Sustainable Chem. Eng.* **2018**, *6*, 11190−11195.

(14) Zhou, S.; Zhang, C.; Liu, J.; Liao, J.; Kong, Y.; Xu, Y.; Chen, G. Formation of an oriented Bi 2 WO 6 photocatalyst induced by in situ Bi reduction and its use for efficient nitrogen fixation. *Catal. Sci. Technol.* **2019**, *9*, 5562−5566.

(15) Shi, H.; Zhang, C.; Zhou, C.; Chen, G. Conversion of CO 2 into renewable fuel over Pt−gC 3 N 4/KNbO 3 composite photocatalyst. *RSC Adv.* **2015**, *5*, 93615−93622.

(16) Zhang, T.; Zhao, K.; Yu, J.; Jin, J.; Qi, Y.; Li, H.; Hou, X.; Liu, G. Photocatalytic water splitting for hydrogen generation on cubic, orthorhombic, and tetragonal KNbO 3 microcubes. *Nanoscale* **2013**, *5*, 8375−8383.

(17) Liu, J.; Li, R.; Zu, X.; Zhang, X.; Wang, Y.; Wang, Y.; Fan, C. Photocatalytic conversion of nitrogen to ammonia with water on triphase interfaces of hydrophilic-hydrophobic composite Bi4O5Br2/ZIF-8. *Chem. Eng. J.* **2019**, *371*, 796−803.

(18) Huang, C.-W.; Nguyen, V.-H.; Zhou, S.-R.; Hsu, S.-Y.; Tan, J.-X.; Wu, K. C.-W. Metal−organic frameworks: preparation and applications in highly efficient heterogeneous photocatalysis. *Sustain. Energy Fuels* **2020**, *4*, 504−521.

(19) Abazari, R.; Morsali, A.; Dubal, D. P. An advanced composite with ultrafast photocatalytic performance for the degradation of antibiotics by natural sunlight without oxidizing the source over TMU-5@ Ni−Ti LDH: mechanistic insight and toxicity assessment. *Inorg. Chem. Front.* **2020**, *7*, 2287−2304.

https://doi.org/10.1021/acs.inorgchem.1c03622
Inorg. Chem. XXXX, XXX, XXX−XXX

(20) Bagheri, M.; Masoomi, M. Y.; Morsali, A. A MoO3−Metal−Organic Framework Composite as a Simultaneous Photocatalyst and Catalyst in the PODS Process of Light Oil. *ACS Catal.* **2017**, *7*, 6949−6956.
(21) Masoomi, M. Y.; Stylianou, K. C.; Morsali, A.; Retailleau, P.; Maspoch, D. Selective CO2 Capture in Metal−Organic Frameworks with Azine-Functionalized Pores Generated by Mechanosynthesis. *Cryst. Growth Des.* **2014**, *14*, 2092−2096.
(22) Yuan, B.; Ma, D.; Wang, X.; Li, Z.; Li, Y.; Liu, H.; He, D. A microporous, moisture-stable, and amine-functionalized metal−organic framework for highly selective separation of CO2 from CH4. *Chem. Commun.* **2012**, *48*, 1135−1137.
(23) Zhu, D.; Zhang, L.; Ruther, R. E.; Hamers, R. J. Photo-illuminated diamond as a solid-state source of solvated electrons in water for nitrogen reduction. *Nat. Mater.* **2013**, *12*, 836−841.
(24) Thommes, M.; Kaneko, K.; Neimark, A. V.; Olivier, J. P.; Rodriguez-Reinoso, F.; Rouquerol, J.; Sing, K. S. Physisorption of gases, with special reference to the evaluation of surface area and pore size distribution (IUPAC Technical Report). *Pure Appl. Chem.* **2015**, *87*, 1051−1069.
(25) Kulaksızoğlu, S.; Gup, R. A new bis (azine) tetradentate ligand and its transition metal complexes: Synthesis, characterisation, and extraction properties. *Chem. Pap.* **2012**, *66*, 194−201.
(26) Clougherty, L.; Sousa, J.; Wyman, G. C= N stretching frequency in infrared spectra of aromatic azomethines. *J. Org. Chem.* **1957**, *22*, 462.
(27) Stratton, W. J.; Busch, D. H. The Complexes of Pyridinaldazine. III. Infrared Spectra and Continued Synthetic Studies. *J. Am. Chem. Soc.* **1960**, *82*, 4834−4839.
(28) Golovina, I. S.; Bryksa, V. P.; Strelchuk, V. V.; Geifman, I. N.; Andriiko, A. A. Size effects in the temperatures of phase transitions in KNbO3 nanopowder. *J. Appl. Phys.* **2013**, *113*, 144103.
(29) Pascual-Gonzalez, C.; Schileo, G.; Khesro, A.; Sterianou, I.; Wang, D.; Reaney, I. M.; Feteira, A. Band gap evolution and a piezoelectric-to-electrostrictive crossover in (1−x) KNbO 3−x (Ba 0.5 Bi 0.5)(Nb 0.5 Zn 0.5) O 3 ceramics. *J. Mater. Chem. C* **2017**, *5*, 1990−1996.
(30) Jia, S.; Su, Y.; Zhang, B.; Zhao, Z.; Li, S.; Zhang, Y.; Li, P.; Xu, M.; Ren, R. Few-layer MoS 2 nanosheet-coated KNbO 3 nanowire heterostructures: piezo-photocatalytic effect enhanced hydrogen production and organic pollutant degradation. *Nanoscale* **2019**, *11*, 7690−7700.
(31) Zhao, S.-N.; Wang, G.; Poelman, D.; Van Der Voort, P. Metal organic frameworks based materials for heterogeneous photocatalysis. *Molecules* **2018**, *23*, 2947.
(32) Shi, W.; Shu, K.; Huang, X.; Ren, H.; Li, M.; Chen, F.; Guo, F. Enhancement of visible-light photocatalytic degradation performance over nitrogen-deficient g-C3N4/KNbO3 heterojunction photocatalyst. *J. Chem. Technol. Biotechnol.* **2020**, *95*, 1476−1486.
(33) H. Khorrami, G.; Kompany, A.; Khorsand Zak, A. Structural and optical properties of (K, Na) NbO3 nanoparticles synthesized by a modified sol−gel method using starch media. *Adv. Powder Technol.* **2015**, *26*, 113−118.
(34) Shalom, M.; Ressnig, D.; Yang, X.; Clavel, G.; Fellinger, T. P.; Antonietti, M. Nickel nitride as an efficient electrocatalyst for water splitting. *J. Mater. Chem. A* **2015**, *3*, 8171−8177.
(35) Maneerung, T.; Hidajat, K.; Kawi, S. K-doped LaNiO3 perovskite for high-temperature water-gas shift of reformate gas: Role of potassium on suppressing methanation. *Int. J. Hydrogen Energy* **2017**, *42*, 9840−9857.
(36) Yu, J.; Chen, Z.; Wang, Y.; Ma, Y.; Feng, Z.; Lin, H.; Wu, Y.; Zhao, L.; He, Y. Synthesis of KNbO 3/gC 3 N 4 composite and its new application in photocatalytic H2 generation under visible light irradiation. *J. Mater. Sci.* **2018**, *53*, 7453−7465.
(37) Ji, Q.; Bi, L.; Zhang, J.; Cao, H.; Zhao, X. S. The role of oxygen vacancies of ABO 3 perovskite oxides in the oxygen reduction reaction. *Energy Environ. Sci.* **2020**, *13*, 1408−1428.
(38) Frederickson, L. D. An Infrared Study of the C= N Stretching Vibration in Azine Derivatives of Aldehydes and Ketones. *Anal. Chem.* **1964**, *36*, 1349−1355.
(39) Adhikari, S.; Kaminsky, W.; Kollipara, M. R. Pyridyl azine Schiff-base ligands exhibiting unexpected bonding modes towards ruthenium, rhodium and iridium half-sandwich complexes: synthesis and structural studies. *J. Organomet. Chem.* **2017**, *836−837*, 8−16.
(40) Lianwei, S.; Xianyou, Z. XPS study on barium lanthanum magnesium niobate. *J. Rare Earths* **2006**, *24*, 310−313.
(41) Dong, C.; Wang, X.; Liu, X.; Yuan, X.; Dong, W.; Cui, H.; Duan, Y.; Huang, F. In situ grown Nb 4 N 5 nanocrystal on nitrogen-doped graphene as a novel anode for lithium ion battery. *RSC Adv.* **2016**, *6*, 81290−81295.
(42) Wang, J.; Wang, X.; Cui, Z.; Liu, B.; Cao, M. One-pot synthesis and Nb 4 N 5 surface modification of Nb 4+ self-doped KNbO 3 nanorods for enhanced visible-light-driven hydrogen production. *Phys. Chem. Chem. Phys.* **2015**, *17*, 14185−14192.

https://doi.org/10.1021/acs.inorgchem.1c03622
Inorg. Chem. XXXX, XXX, XXX−XXX